Small

NANO · MICRO small
www.small-journal.com

RESEARCH ARTICLE

Rational Synthesis of Extended π-Conjugated Covalent Organic Frameworks for Enhanced Photocatalytic Uranium(VI) Removal

Juyao Zhang[1] | Mengjie Hao[1] | Xinyue Zhang[1] | Muliang Xiao[1] | Yinghui Xie[1] | Ruining Cao[1] | He Gu[1] | Xiaolu Liu[1] | Hui Yang[1] | Geoffrey I. N. Waterhouse[2] | Shengqian Ma[3] | Xiangke Wang[1]

[1]College of Environmental Science and Engineering, North China Electric Power University, Beijing, China | [2]School of Chemical Sciences, The University of Auckland, Auckland, New Zealand | [3]Department of Chemistry, University of North Texas, Denton, Texas, USA

Correspondence: Hui Yang (h.yang@ncepu.edu.cn) | Shengqian Ma (shengqian.ma@unt.edu) | Xiangke Wang (xkwang@ncepu.edu.cn)

Received: 3 March 2026 | **Revised:** 17 June 2026 | **Accepted:** 24 June 2026

Keywords: $(UO_2)O_2{\cdot}4H_2O$ | covalent organic frameworks | extended π-conjugation | one-pot method | photocatalysis

ABSTRACT

Atom-level control of π-conjugations in covalent organic frameworks (COFs) facilitates deep exploration of the relationship between electron-transport properties and photocatalysis, which is particularly important for improving photocatalytic performance. Herein, we present a comprehensive strategy for the synthesis of extended π-conjugated COFs via a one-pot tandem Scholl cyclization-dehydrogenation reaction. The extended π-conjugated COFs are constructed by planar covalent bonds, in which imine linkers are converted to imine-cyclized counterparts, resulting in all chemical bonds conjugatively connected throughout the framework. Subsequently, benzene units are substituted with naphthalene units to yield an even more highly extended π-conjugated framework. These approaches ensure that delocalized electrons efficiently transport across the COF framework with extended π-conjugation, resulting in extended-range light absorption, improved electron-hole separation, and more efficient charge-carrier utilization under visible-light irradiation. Notably, the extended π-conjugated COFs exhibit remarkable photocatalytic performance in uranium(VI) removal from contaminated water sources, surpassing the performance of electron-deficient p-π-conjugated counterparts. These findings demonstrate a new general design strategy for the synthesis of highly-conjugated COF photocatalysts. The strategy is expected to provide new insights into the rational design of high-performance COFs for applications in photocatalysis, including water-source decontamination and potentially numerous other applications.

1 | Introduction

Covalent organic frameworks (COFs) represent a class of crystalline porous polymers composed of organic building blocks interconnected through covalent bonds to form conjugated networks [1–3]. Rational pre-design strategies impart COFs with structural tunability [4–6], large specific surface areas [7–9], and excellent chemical stability [10, 11], rendering them exceptionally versatile for a wide range of applications [12–16]. Recently, COFs have emerged as an ideal platform for photocatalysts due to their well-defined planar π-conjugated systems and high electron-transport capabilities. The structural advantages allow for the tuning of the visible-light absorption bands [17–20], efficient electron-hole separation [21–24], and facile photogenerated carrier production [25], resulting in good photocatalytic activity. However, the biggest challenge for COF photocatalysts lies in efficiently utilizing photogenerated charges, which depends on their building blocks and linkers [26–28]. The charge carriers are

© 2026 Wiley-VCH GmbH

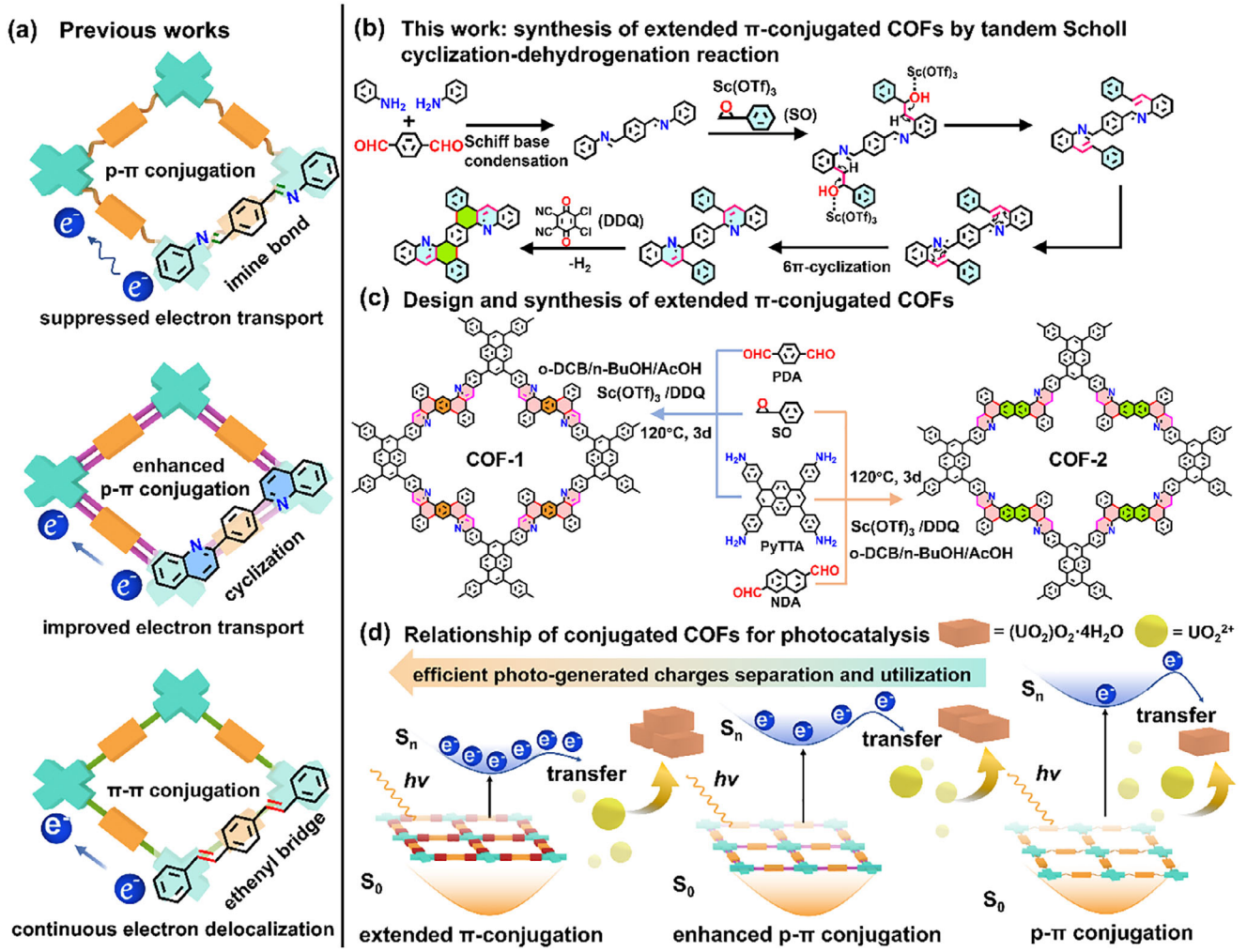


FIGURE 1 | (a) Schematic diagram of different types of conjugation in COFs. (b) One-pot tandem Scholl cyclization-dehydrogenation reaction used to prepare extended π-conjugated COFs. (c) Design and synthesis of extended π-conjugated COFs. (d) Schematic illustration of the relationship between π-conjugation and photocatalytic performance in COFs.

generally confined within adjacent building blocks and knots, leading to rapid electron-hole recombination and short-lived excited states [29]. To improve the utilization of charge carriers, enhancing π-conjugation in COFs is indispensable, thereby driving dissociated charge carriers to disperse over large regions and preventing recombination [30]. Consequently, the regulation of conjugated structures to boost photocatalytic performance has attracted widespread attention from researchers [31–34]. The synthesis of COFs relies on dynamic covalent chemistry processes such as imine condensation between aldehyde- and amino-linkers that confer stability [35, 36]. Nevertheless, the inherent flexibility of imine bonds imposes limitations that inhibit long-range charge delocalization within local conjugated structures, thereby impeding the overall photocatalytic performance of COFs [37]. Therefore, converting or reinforcing these bonds represents a general approach for effectively constructing and maintaining extended planar π-conjugated frameworks.

Pioneering studies have demonstrated that the cleavage and formation of chemical bonds are fundamental to the development of conjugated COFs. These structures achieve through-bond conjugation via bond connections, directly constructing p-π or π-π conjugation through overlapping orbitals (Figure 1a) [38–40]. Given that imine bonds inhibit electron transfer, researchers have explored various strategies to enhance p-π conjugation, thereby promoting electron transfer capabilities and photocatalytic activity [41]. For example, the irreversible formation of aromatic benzoxazole joints enhanced covalent linkages, benefiting the π-conjugation of crystalline framework and photocatalytic activity [42]. The imine bonds were eliminated by post-synthetic modification, transforming propenyloxy groups into chemically stable chromenoquinoline rings that increased π-conjugation of the frameworks, thereby creating novel donor-acceptor systems and COFs with greatly enhanced photocatalytic activity [43]. Moreover, the crystalline thiadiazole-linked TDA-COF was synthesized via thionation, cyclization, and oxidation of N-acylhydrazole bonds, thereby providing a new method for the fabrication of π-conjugated COFs [44]. Compared with parent COFs, thiadiazole-linked COFs promote π-electron delocalization throughout the reticular framework, resulting in excellent photocatalytic H_2 evolution performance. Moreover, constructing π-π conjugated COFs represents another viable approach for improving electronic transport and photocatalytic efficiency (Figure 1a) [45]. The conjugated C═C bond present in

sp^2c-COF allows continuous overlap of π orbitals within the 2D framework, significantly enhancing both π-π conjugation and electron delocalization. This leads to a narrowed band gap, broadened visible-light absorption, and boosted carrier mobility, thus its performance exceeds that of partially conjugated structures such as imine- or hydrazone-COFs [46]. The synthesis of π-π-conjugated COFs was achieved by incorporating an ethenyl group (—CH═CH—) directly linked to the benzene ring via a sp^2-hybridized carbon atom. This configuration forms a continuous electron-delocalization system that promotes efficient electron transport and allows a high photocatalytic hydrogen production rate [47]. Additionally, a p-π conjugated COF was developed by transforming imine-linked COFs into thieno [3,2-c] pyridine linkages. This conjugated system combines an electron-rich thiophene unit with an electron-deficient pyridine unit to enhance p-π conjunction. The improved overlap of p-orbitals facilitates effective electron delocalization and charge carrier mobility, significantly boosting photocatalytic performance [48]. Although these previous studies represent significant advancements in COF photocatalysts, the impact of conjugated structures, particularly planar π-conjugation, on electron transport and delocalization at the atomic level has yet to be reported, warranting further exploration. Translating this paradigm into π-extended functional frameworks poses considerable challenges due to: (i) the inherent conflict between conformational flexibility required for reversible self-assembly and structural rigidity necessary for extended π-conjugation; (ii) the multi-step intermediates or post-synthesis processes typical of molecular editing that often risk the integrity of the framework. Therefore, the exploration of extended π-conjugated COFs is highly sought after but challenging.

Herein, we propose a new strategy for the design of extended π-conjugated COFs aimed at improving photocatalytic activity through control of conjugation to optimize electron transport and delocalization (Figure 1b,c). In brief, extended π-conjugated COF-1 was designed and synthesized via a one-pot tandem Scholl cyclization-dehydrogenation reaction. Subsequently, benzene units were substituted with naphthalene units to yield COF-2, resulting in an even more highly extended π-conjugated framework. The imine-cyclized (COF-3 and COF-4) and imine-linked (COF-5 and COF-6) COFs with p-π conjugation were synthesized using Scholl cyclization approaches, respectively (Figure S1). While the structural characteristics of these homologous COFs may appear similar at first glance, there are significant differences in the connectivity of chemical bonds at the molecular level, which profoundly affect the type and degree of conjugation. COF-1 and COF-2 with extended π-conjugated frameworks facilitate continuous π-electron delocalization and efficient electron transport by replacing traditional electron-deficient p-π conjugated structures with polycyclic aromatic units (Figure 1d). This methodology demonstrates a high-speed pathway for electron transport while preserving an extended carrier lifetime. Building on this synthetic success, we systematically investigated the relationship between the π-electron delocalization properties of the synthesized COFs, including those featuring structurally corresponding p-π conjugation and extended π-conjugation under visible-light irradiation alongside their photocatalytic performance. We employed photocatalytic removal of uranyl (UO_2^{2+}) from contaminated water as a test reaction. The extended π-conjugated COF-1 and COF-2 exhibited exceptional photocatalytic efficiency in the removal of uranyl from contaminated water sources, surpassing their corresponding imine-linked counterparts, as well as imine-cyclized structures with electron-deficient p-π conjugation. The extended π-conjugated COFs developed in this study offer a new strategy for creating high-performance photocatalysts for uranyl removal and other applications.

2 | Results and Discussion

2.1 | Design, Synthesis, and Characterization of COFs

Figure 1c shows the general synthetic route adopted in this study for the preparation of extended π-conjugated COF-1 and COF-2 through a one-pot tandem Scholl cyclization-dehydrogenation reaction. We reacted 4,4′,4′′,4′′′-(pyrene-1,3,6,8-tetrayl)tetraaniline (PyTTA), 1,4-phthalaldehyde (PDA), styrene oxide (SO), $Sc(OTf)_3$, and 2,3-dichloro-5,6-dicyano-1,4-benzoquinone (DDQ) in a mixture of dichlorobenzene (o-DCB)/n-butanol (n-BuOH)/acetic acid (AcOH) (5:5:1, by volume) at 120°C for 3 days. Following filtration and washing with methanol and acetone, the powder designated as COF-1 was obtained. COF-2 was obtained via a similar synthetic route to COF-1, with the PDA linker replaced by the naphthalene-2,6-dicarbaldehyde (NDA) linker. The chemical structural components of both COF-1 and COF-2 were subsequently analyzed using Fourier-transform infrared spectroscopy (FT-IR) and solid-state cross-polarization magic angle spinning nuclear magnetic resonance (^{13}C CP/MAS NMR) measurements. The FT-IR spectra showed strong absorption bands around ~1525 cm^{-1} in both COF-1 and COF-2, verifying the formation of quinoline rings [49–51] within the frameworks and indicating successful cyclization along with the emergence of π-conjugated structures (Figure 2a). Moreover, their FT-IR spectra displayed the disappearance of the characteristic N-H stretching band at ~3340 cm^{-1} of PyTTA and the aldehydic C = O stretching bands at ~1690 cm^{-1} of PDA and NDA, demonstrating the successful formation of frameworks. The solid-state ^{13}C NMR spectra for both COF-1 and COF-2 showed the characteristic resonance at ~140 ppm, assigned to the quinoline ring of extended π-conjugated structures (Figure 2b).

Next, powder X-ray diffraction (PXRD) and Pawley refinement analysis were used to investigate the crystallinity of COF-1 and COF-2. The experimental PXRD showed that COF-1 possessed a crystalline structure with diffraction peaks at 2θ = ~3.8, 5.3, 7.5, and 11.3°, corresponding to the (110), (200), (220), and (420) crystal reflections (Figure 2c). Using Materials Studio software, we established a reasonable theoretical crystal structure for the eclipsed AA stacking model to simulate the experimental PXRD patterns (Figure 2d). Pawley refinement further revealed that COF-1 crystallized in the C2/M space group with monoclinic lattice parameters of a = 36.22 Å, b = 32.10 Å, c = 3.88 Å, α = 90°, β = 81.85°, and γ = 90°. The agreement factors of R_p = 4.09% and R_{wp} = 5.31% were obtained (Figure 2c; Table S1). To optimize the synthesis of COF-1, we prepared samples under varying synthetic conditions, with the corresponding XRD patterns compared in Figure S2. The findings confirm that the reported synthetic route yields COF-1 with high crystallinity, evidencing a near-optimal

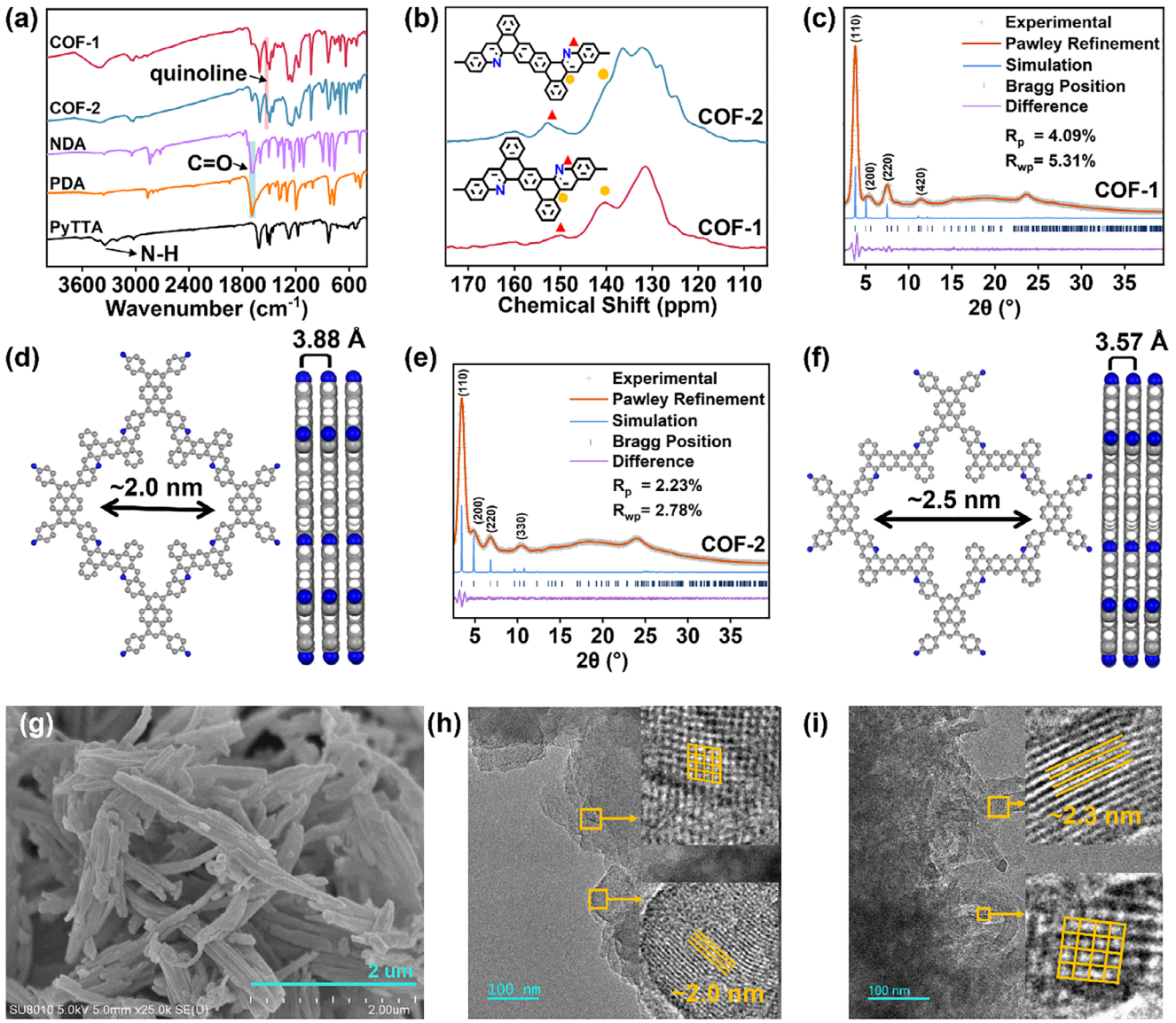


FIGURE 2 | Characterization of synthesized COFs. (a) FT-IR spectra for PyTTA, PDA, NDA COF-1, and COF-2. (b) Solid-state ^{13}C CP/MAS NMR spectra of COF-1 and COF-2. (c), (e) Experimental PXRD patterns of COF-1, COF-2 with corresponding Pawley refinement (orange), simulated results (light blue), and Bragg positions (blue) showing a good fit for the experimental data (gray) with minimal differences (purple). (d), (f) Top and side views of the eclipsed AA stacking crystal structure of COF-1 and COF-2. The C, N, and H atoms are represented by gray, blue, and white spheres, respectively. (g) SEM image of COF-1. (h), (i) HRTEM images of COF-1 and COF-2 (insets highlight the honeycomb-like pores and channels).

synthetic protocol. Similarly, the experimental PXRD of COF-2 possessed a crystalline structure with diffraction peaks at 2θ = ~3.4, 4.8, 6.8, and 10.2° corresponding to the (110), (200), (220), and (330) Bragg peaks of a lattice with CMM2 symmetry. Pawley refinement yielded an orthorhombic unit cell parameters of a = 36.82 Å, b = 36.90 Å, and c = 3.57 Å with $\alpha = \beta = \gamma = 90°$, resulting in agreement factors of R_{wp} = 2.78%, R_p = 2.23% (Figure 2e, Table S2). On the basis of these results, COF-1 and COF-2 possessed 2D structures featuring honeycomb-like pores with theoretical dynamic pore sizes of ~2.0 and 2.5 nm, respectively (Figure 2d,f). Scanning electron microscopy (SEM) images showed that COF-1 and COF-2 crystallized with nanorod-like structures (Figure 2g; Figure S3). High-resolution transmission electron microscopy (HRTEM) images of COF-1 and COF-2 revealed lattice fringes with spacings of ~2.0 nm and 2.3 nm, respectively, in accordance with their theoretical results (Figure 2h,i). COF-2 exhibited a larger pore size than COF-1 due to the NDA linker being longer than the PDA linker. The porosities of COF-1 and COF-2 were determined by measuring N_2 sorption isotherms on activated samples at 77 K. The adsorption-desorption isotherms for both COFs displayed type II curves, indicating the presence of mesopores in both structures (Figure 3a). The Brunauer-Emmett-Teller (BET) surface areas were calculated to be 635.0 and 701.6 m^2/g for COF-1 and COF-2, respectively. The pore size distribution analyses verified that pore diameters clustered at 1.4-2.0 and 1.7–2.2 nm, respectively, using the density function theory (DFT) model, consistent with the HRTEM results and theoretical values from structural simulations, and in good general agreement with the predicted apertures in the simulated structures (Figure 3b). The ordered alignment with high crystallinity and pore size in COF-1 and COF-2 suggests the successful construction of extended π-conjugated structures.

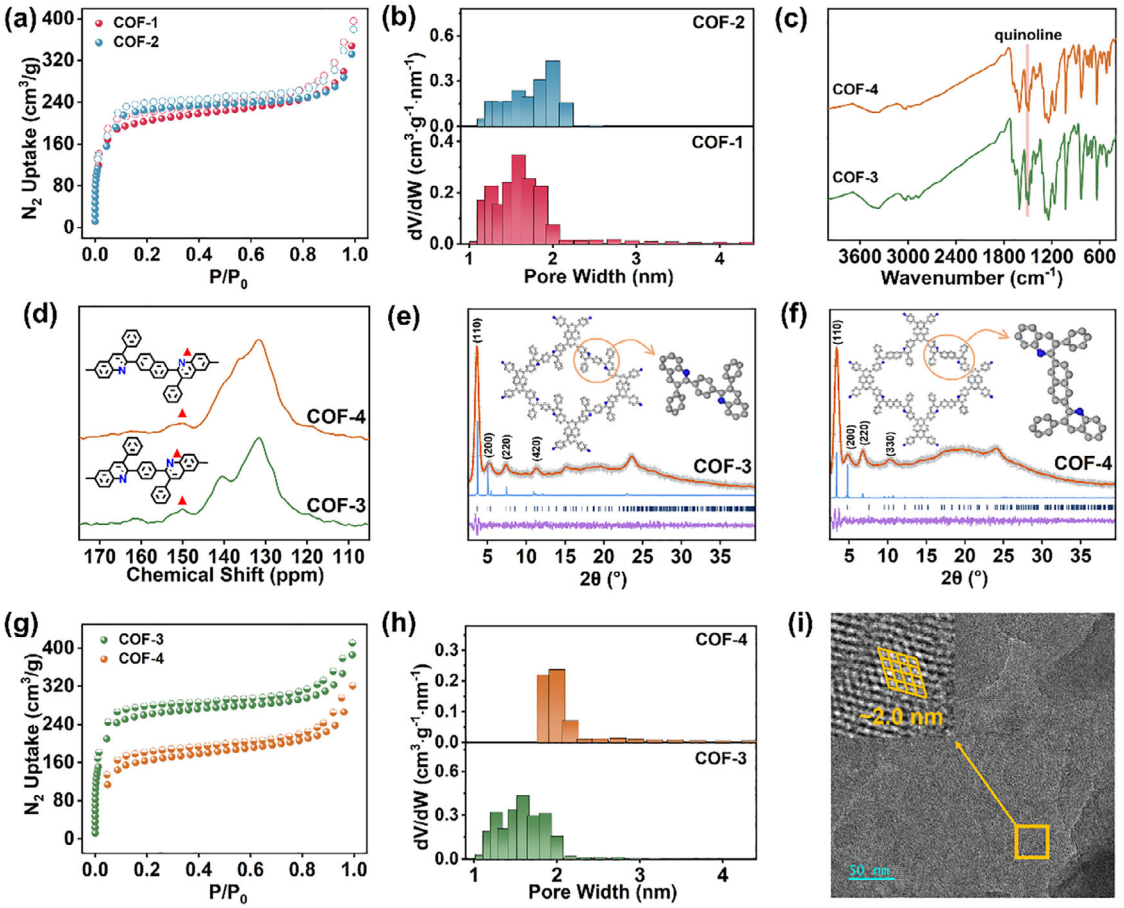


FIGURE 3 | Characterization of synthesized COFs. (a) N_2 sorption isotherms measured at 77 K for COF-1 and COF-2. (b) Pore size distributions of COF-1 and COF-2 from N_2 isotherms measured at 77 K. (c) FT-IR spectra for COF-3 and COF-4. (d) Solid-state ^{13}C CP/MAS NMR spectra of COF-3 and COF-4. (e), (f) Experimental PXRD patterns of COF-3, COF-4 with corresponding Pawley refinement (orange), simulated results (light blue), and Bragg positions (blue) showing a good fit for the experimental data (gray) with minimal differences (purple). The inset shows the structural fragments of COF-3 and COF-4, assuming the eclipsed AA stacking mode. (g) N_2 sorption isotherms measured at 77 K for COF-3 and COF-4. (h) Pore size distributions of COF-3 and COF-4 from N_2 isotherms measured at 77 K. (i) HRTEM image of COF-3 (insets highlight the honeycomb-like pores and channels).

The structural conjugation of COFs significantly influences their photocatalytic performance [52]. Encouraged by the results above, we next sought to study the relationships between structural conjugation and photocatalytic activity of COFs at the molecular level. Accordingly, we also synthesized electron-deficient p-π-conjugated COFs (from COF-3 to COF-6, counterparts of COF-1 and COF-2). COF-3 and COF-4 were synthesized using the same process as for COF-1 and COF-2, without the addition of DDQ (Figure S1). Similar to COF-1 and COF-2, solid-state ^{13}C CP-MAS NMR and FT-IR analyses confirmed the presence of quinoline units in both COF-3 and COF-4 (Figure 3c,d). The FT-IR spectra exhibited characteristic quinolone peaks at 1525 cm^{-1} for both COF-3 and COF-4, confirming that styrene oxide reacted with the imine groups to form quinolones through a Povarov reaction (Figure 3c). The ^{13}C CP/MAS NMR spectra of COF-3 and COF-4 showed a peak with a chemical shift of ~150 ppm, further confirming the presence of quinolones, consistent with the proposed structures (Figure 3d). Based on PXRD combined with structural simulations, the corresponding unit cell parameters were obtained with $a = 35.43$ Å, $b = 32.28$ Å, $c = 3.88$ Å, $\alpha = 90°$, $\beta = 81.85°$, and $\gamma = 90°$ (with agreement factors of $R_p = 3.95\%$ and $R_{wp} = 4.95\%$) for COF-3, and $a = 36.83$ Å, $b = 36.91$ Å, $c = 3.57$ Å, $\alpha = \beta = \gamma = 90°$ (with agreement factors of $R_{wp} = 1.17\%$, $R_p = 0.90\%$) for COF-4 (Table S3 and S4). Results confirmed COF-3 and COF-4 possessed rhombic channels running along the crystallographic *c-axis* with estimated pore sizes of 2.0 nm and 2.4 nm, respectively (Figure 3e,f). The N_2 sorption isotherms of COF-3 and COF-4 were measured at 77 K, yielding BET surface areas of 798.6 and 517.0 m^2/g, respectively (Figure 3g). Fitting the isotherm using DFT yielded pore size distributions with maxima of 1.4-2.0 and 1.8–2.2 nm for COF-3 and COF-4, respectively (Figure 3h). SEM and HRTEM images revealed that the individual microspheres were composed of smaller nanorods (Figure 3i; Figure S4–S6). These results revealed that the p-π-conjugated COF-3 and COF-4 were successfully constructed.

To validate the utility of extended π-conjugation for enhanced photocatalytic activity, we synthesized [4 + 2] imine-linked COF-5 and COF-6 by condensation of PyTTA with PDA or NDA using acetic acid as the catalyst in a mixture of o-DCB/n-BuOH at 120°C for 3 days (Figure S1). The synthesis and characterization data for COF-6 are provided in the supplemental information (Figure S1, S7–S14 and Table S5 and S6). COF-5 and COF-6 contain p-π conjugations. Next, we conducted chemical stability tests on the

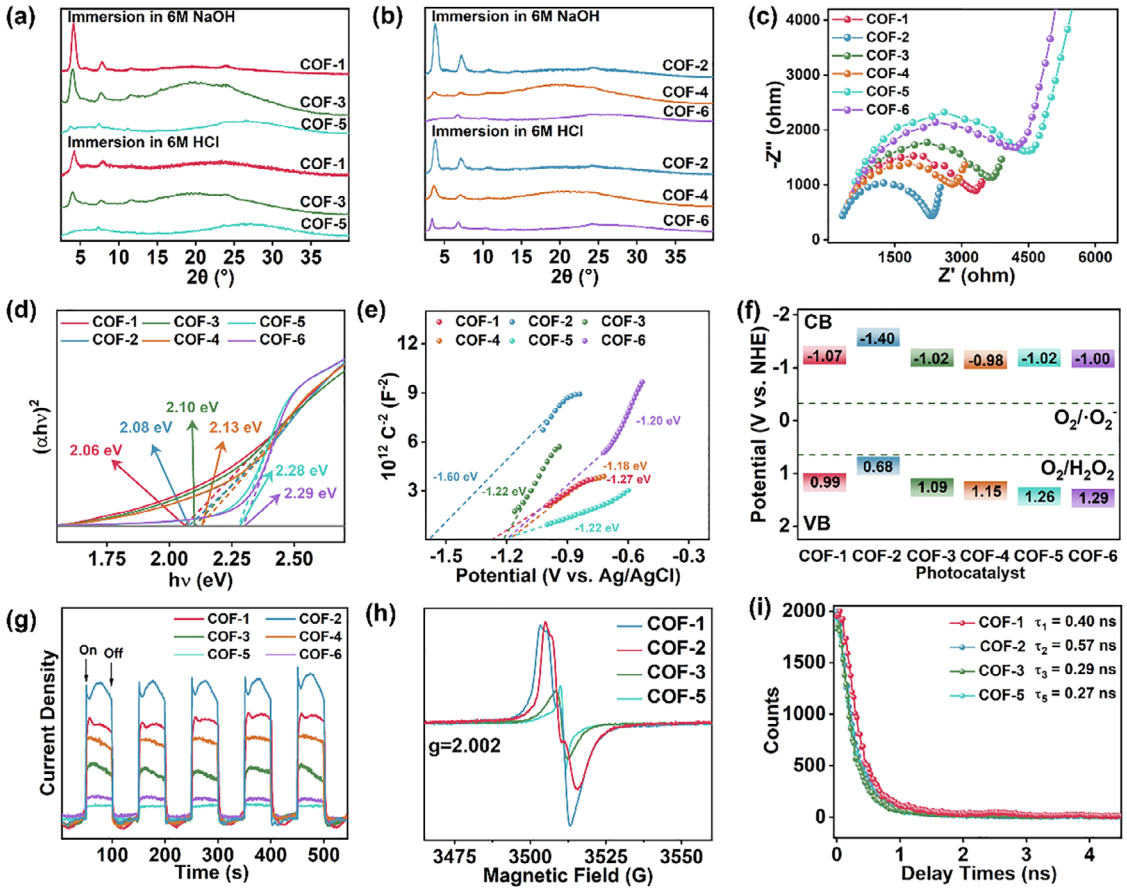


FIGURE 4 | Physical and photoelectrochemical characterization of synthesized COFs. (a) Experimental PXRD patterns of COF-1, COF-3, and COF-5 after immersion in 6 M NaOH and 6 M HCl solution. (b) Experimental PXRD patterns of COF-2, COF-4, and COF-6 after immersion in 6 M NaOH and 6 M HCl solution. (c) EIS spectra for COF-1 to COF-6. (d) Tauc plots for COF-1 to COF-6. (e) Mott-Schottky plots for COF-1 to COF-6. (f) Band alignments for COF-1 to COF-6. (g) Photocurrent responses for COF-1 to COF-6. (h) EPR conduction band e-signals for COF-1, COF-2, COF-3, and COF-5. (i) Photoluminescence decay curves for COF-1, COF-2, COF-3, and COF-5.

COFs by immersing the powder samples in 6 M NaOH or 6 M HCl solutions. After 3 days, the powder samples were collected, rinsed repeatedly with deionized water, and subsequently characterized by PXRD (Figure 4a,b). Negligible changes in the characteristic PXRD peaks of COF-1 and COF-2 were observed after these treatments, indicating that the COFs possess excellent chemical stability. The post-treatment diffraction peak intensities of COF-3 and COF-4 decreased somewhat, suggesting that their chemical stability was not as good as that of COF-1 and COF-2. COF-5 and COF-6 showed poor stability under similar conditions. The results revealed that the extended π-conjugation of COF-1 and COF-2 improved their chemical stability.

2.2 | Photophysical and Electrochemical Properties

We systematically investigated the photophysical and electrochemical properties of the various COFs (through COF-1 to COF-6) using electrochemical impedance spectroscopy (EIS), UV/Vis diffuse reflectance spectroscopy (UV/Vis DRS), electron paramagnetic resonance (EPR) spectroscopy, transient photocurrent, and time-resolved photoluminescence (TRPL). EIS was performed to investigate the charge transport properties of the COFs. COF-1 and COF-2 exhibited smaller semicircles in the Nyquist plots, indicating lower charge-transfer resistance and more efficient charge-carrier separation and transport (Figure 4c). The COFs demonstrated absorption between 420 and 800 nm, signifying their excellent visible-light-harvesting abilities (Figure S15). The optical band gap energies determined from the Tauc plots were found to be 2.06, 2.08, 2.10, 2.13, 2.28, and 2.29 eV for COF-1, COF-2, COF-3, COF-4, COF-5, and COF-6, respectively (Figure 4d). These narrow band gap energies suggest that the COF photocatalysts should offer good visible light-driven photocatalytic activity. COF-1 (COF-2) has a narrower bandgap than both COF-3 (COF-4) and COF-5 (COF-6), suggesting that extended π-conjugation reduces the bandgap and enhances visible-light absorption for homologous COFs. Next, we conducted Mott-Schottky tests to determine the valence-band (VB) and conduction-band (CB) positions of the COFs. Shown in Figure 4e and Figure S16–S21, the Mott-Schottky plots of the COFs (C^{-2} vs. E) display a typical positive slope characteristic of n-type semiconductors. The flat-band potentials (E_{fb}, vs. Ag/AgCl) for COF-1 to COF-6 were determined to be −1.27, −1.60, −1.22, −1.18, −1.22, and −1.20 eV, respectively. Based on this data and the previously calculated band gaps, the VB and CB edges were determined. In general, the reducing ability of a photocatalyst is usually related to its CB potential, while the oxidizing ability

depends on its VB potential. It is evident that extended π-conjugated COF-1 and COF-2 exhibit much better reducing ability (more negative CB potentials), which arises from continuous π-electron delocalization across the planar polycyclic aromatic network, as shown in Figure 4f. In contrast, COF-3 and COF-4 contain non-planar quinoline linkages that disrupt long-range orbital overlap, while COF-5 and COF-6 rely on less effective p-π conjugation through imine bonds. Photocurrent measurements were further performed to evaluate the photoelectric responses of COF-1 to COF-6 (Figure 4g). Anodic photocurrents were observed in all tested samples under chopped-light irradiation (on/off cycles). Notably, higher photo responses were recorded from both extended π-conjugated COF-1 and COF-2 compared with those from imine-linked and imine-cyclized structures (through COF-3 to COF-6), suggesting that extended conjugated architectures within these frameworks may substantially improve interfacial charge-transfer rates. The EPR results for all COFs displayed signals around $g = 2.002$, indicating the formation of excited-state electrons under visible-light excitation (Figure 4h). TRPL spectroscopy measurements on the COFs were also carried out to evaluate their photogenerated charge-carrier utilization efficiency (Figure 4i). The calculated average fluorescence lifetimes of COF-1 and COF-2 were 0.40 ns and 0.57 ns, respectively, higher than those of COF-3 (0.29 ns) and COF-5 (0.27 ns), suggesting lower recombination rates of photogenerated charge carriers in extended π-conjugated COFs.

Based on the well-defined structures, large porosity, strong visible-light absorption, and excellent charge separation and transport properties of the COFs developed above, we then conducted photocatalytic studies to explore the effects of different conjugated structures on photocatalytic performance. As proof-of-concept, we performed a series of photocatalytic experiments to assess the viability of the COFs for the removal of uranyl [U(VI)] from contaminated water.

2.3 | Photocatalytic U(VI) Removal Performance

Nuclear fission reactors produce abundant electricity with near zero carbon emissions, making nuclear energy a valuable energy source on the road towards carbon neutrality in the energy sector [53–55]. However, uranium leakage in nuclear accidents and mining activities generates a continuous threat to human health, leading to various radiation-related diseases such as organ lesions, inflammation, and cancer [56, 57]. The dual pressures of resource sustainability and environmental safety have driven the development of high-performance U(VI)-removal materials and catalytic technologies for U(VI) extraction from wastewater [58]. This is aimed at achieving safe, efficient removal of uranium from complex environmental media, such as mining wastes and contaminated water bodies. Encouraged by differences in conjugated structures and the favorable photophysical and electrochemical properties, we investigated the photocatalytic activities of COF-1 to COF-6 with different types of conjugation for uranium removal from contaminated water sources and explored their structure-photocatalytic activity relationships. Initially, we evaluated the photocatalytic performance of these COF photocatalysts in a ~20 ppm uranyl solution. As shown in Figure 5a, COF-2 exhibited the highest uranium removal rate among all tested COFs, achieving a removal efficiency exceeding 99% after 8 h. In comparison, COF-1 demonstrated a slightly lower U(VI) removal efficiency, approximately 90%, under similar experimental conditions. The U(VI) removal efficiencies for COF-3, COF-4, COF-5, and COF-6 were ~50%, 61%, 41%, and 43%, respectively, significantly lower than those observed for COF-1 and COF-2. Furthermore, we evaluated the photocatalytic performance of these materials in uranyl-contaminated (~20 ppm of U(VI)) groundwater (Figure 5b). Consistent with expectations, the U(VI) removal efficiencies followed this order: COF-2> COF-1> COF-4> COF-3> COF-6 ≈ COF-5. Given that both COF-1 and COF-2 displayed excellent photocatalytic activity for U(VI) removal, we subsequently evaluated their uranyl removal performance in U(VI)-containing organic wastewater. Both COF-1 and COF-2 possessed high U(VI) removal efficiencies, with COF-1 and COF-2 achieving a removal ability of ~5 mg/g (>99%), 10 mg/g (>99%) and 20 mg/g (>99%) under an organic-to-U(VI) ratios of 4000, 2000, and 1000, respectively, within 480 min (Figure 5c). Following U(VI) uptake, COF-2 could be readily regenerated by elution with a Na_2CO_3 solution, with a U(VI) removal efficiency of >90% being maintained after five reuse cycles, confirming its good durability (Figure 5d). The virtually identical FT-IR spectra and PXRD patterns of COF-2 before and after cycling attest to its superior stability with no structural degradation (Figure S22 and S23). To investigate the effects of pH on U(VI) removal performance, we examined the photocatalytic activity of the COFs in ~20 ppm uranyl solution over a pH range of 1 to 7. As shown in Figure 5e, COF-2 exhibits a consistently high U(VI) removal efficiency (>99%) at a pH range of 4 to 7. However, due to competition from H^+ with UO_2^{2+} in acidic solutions, the U(VI) removal efficiency drops sharply to approximately 29% at pH 3 and below [59]. This drop in U(VI) removal efficiency is explained by a switch in the surface charge of the COFs from negatively charged at neutral pH to highly positively charged at pH 3 and below, as seen in the zeta potential data for COF-1, COF-2, COF-3, and COF-5 (Figure 5f). The zeta potential results indicate that the COFs carry negative charges at pH 5–9, allowing efficient binding of uranyl cations and thereby boosting photocatalytic activity at near-neutral pH values. These findings underscore the exceptional photocatalytic properties of extended π-conjugated COF-1 and COF-2 for the effective removal of U(VI) from contaminated water sources.

2.4 | Photocatalytic Mechanism Studies

We next conducted comprehensive experimental studies and theoretical calculations on these COFs to gain deeper insights into their photocatalytic mechanisms for U(VI) removal and to explore electron transport and transfer pathways under visible-light irradiation. Techniques such as X-ray photoelectron spectroscopy (XPS), HRTEM, and PXRD were employed to investigate the photocatalytic-generated products of U(VI) removal on COF-2. The U 4f XPS spectra after photocatalysis showed peaks at binding energies of 382.38 and 393.23 eV in a 4:3 (Figure 5g), which could readily be assigned to the U $4f_{7/2}$ and U $4f_{5/2}$ signals, respectively, of a hexavalent U(VI) species [60]. A further set of peaks observed at higher binding energies was assigned to "shake-up" satellites. Morphological characterization through HRTEM revealed that crystalline nanoparticles were formed on the surface of COF-2 during photocatalysis (Figure 5h). Lattice fringes with a d-spacing of ~3.2 Å were observed, corresponding to the (111)

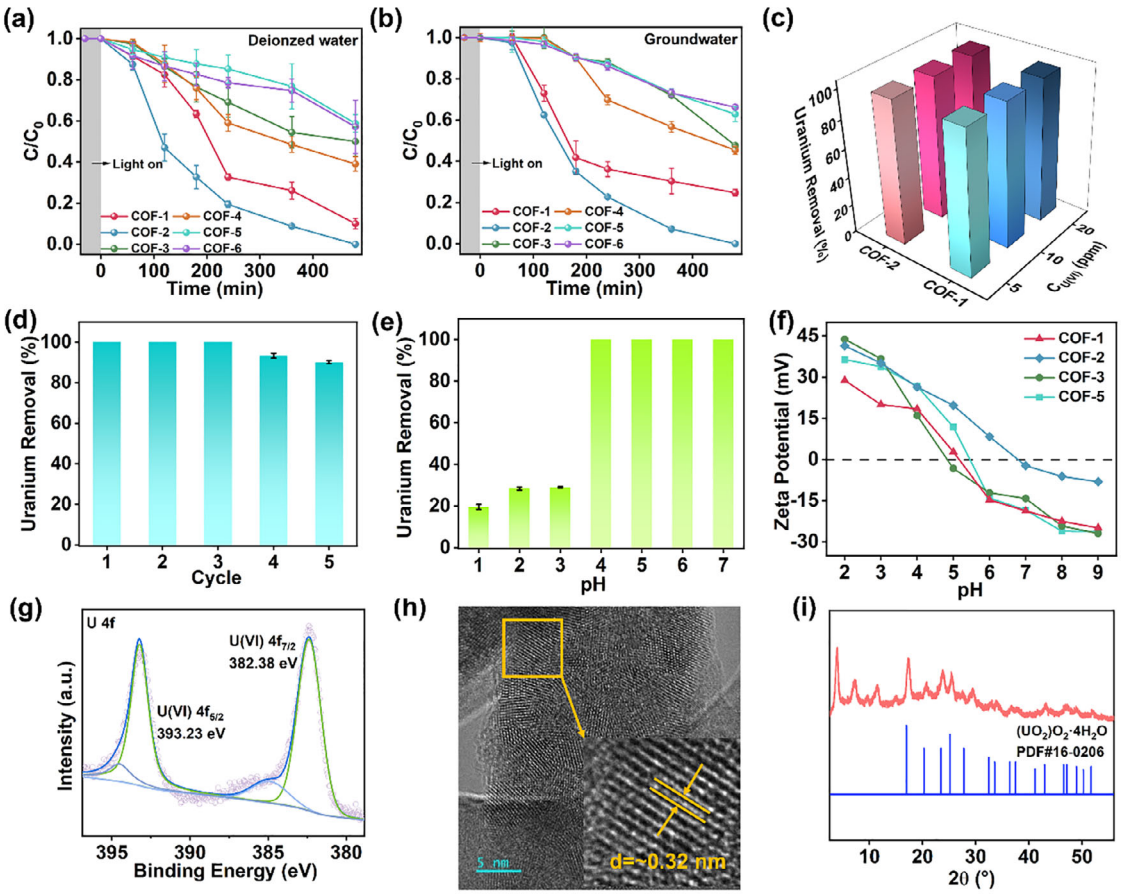


FIGURE 5 | Uranium extraction capacity and product analysis. (a), (b) Uranium extraction from uranyl-spiked deionized water and uranyl-spiked groundwater with initial uranium concentrations of ~20 ppm, using COF-1 to COF-6 as photocatalysts. (c) Uranium extraction from uranyl-spiked organic wastewater with different initial uranium concentrations, using COF-1 and COF-2 as photocatalysts. (d) Uranium cycle extraction from uranyl-spiked groundwater with initial uranium concentrations of ~20 ppm, using COF-2. (e) Removal efficiency of uranium by COF-2 under pH conditions ranging from 1 to 7. (f) Zeta potentials of COF-1, COF-2, COF-3, and COF-5. (g) U 4f XPS spectrum of COF-2 after photocatalysis. (h) HRTEM image of COF-2 after photocatalysis (inset highlights the lattice fringes). (i) PXRD pattern of COF-2 after photocatalysis.

plane of $(UO_2)O_2{\cdot}4H_2O$ [61]. Subsequently, we performed U(VI) removal experiments using a ~50 ppm uranyl solution, yielding a pale-yellow powder that confirmed the presence of U(VI)-containing products on COF-2. The PXRD results showed new 2θ peaks compared with the standard PDF data (PDF#16-0206), which closely align with the standard pattern for $(UO_2)O_2{\cdot}4H_2O$. (Figure 5i) [61].

The above findings suggest that H_2O_2 generation is expected to play an important role in the photocatalytic removal of uranyl and in the formation of $(UO_2)O_2{\cdot}4H_2O$. Therefore, we monitored H_2O_2 production by COF-2 over time under visible-light irradiation in deionized water. As shown in Figure 6a, the H_2O_2 production rates were measured and calculated to be 173.1, 187.1, 56.0, 24.1, 15.8, and 17.1 $\mu mol{\bullet}h^{-1}{\bullet}g^{-1}$ for COF-1 to COF-6, respectively. The relative photocatalytic H_2O_2 production rates are consistent with their performance in the photocatalytic removal of uranyl. We next performed radical-burst experiments to investigate the pathways for both H_2O_2 and $(UO_2)O_2{\cdot}4H_2O$ production. Our findings revealed that uranyl removal by COF-2 decreased from ~99% to ~48.5% and ~61.3% when $AgNO_3$ and p-benzoquinone (p-BQ) were used as electron and superoxide radicals ($\cdot O_2^-$) scavengers, respectively (under an air atmosphere) (Figure 6b) [62]. No significant removal of uranyl ions was observed in photocatalytic tests with N_2 purging, confirming that oxygen is required for efficient photocatalytic uranium removal. The results confirm that H_2O_2 is produced via photogenerated electrons reacting with dissolved O_2, thereby validating that the photocatalytic oxygen reduction reaction (ORR) is the predominant pathway for H_2O_2 generation by these COFs. We identified radical formation by these COFs during photocatalytic processes under visible-light irradiation using EPR. As anticipated, $\cdot O_2^-$ was successfully trapped and detected by employing 3,4-dihydro-2,3-dimethyl-2H-pyrrole 1-oxide (DMPO) as a trapping agent under visible light conditions (Figure 6c) [63]. The above results confirm that H_2O_2 is produced via photogenerated electrons reacting with dissolved O_2, thereby validating that the photocatalytic ORR progress is the predominant pathway for H_2O_2 generation by these COFs. In summary, we propose that the H_2O_2 production leads to the subsequent formation of solid $(UO_2)O_2{\cdot}4H_2O$ by the following route: $UO_2^{2+} + 4H_2O + H_2O_2 \rightarrow (UO_2)O_2{\cdot}4H_2O\,(s) + 2H^+$ [64].

Based on the aforementioned experimental results, we subsequently performed DFT calculations to gain deeper insights into the mechanisms underlying photocatalysis and to investigate

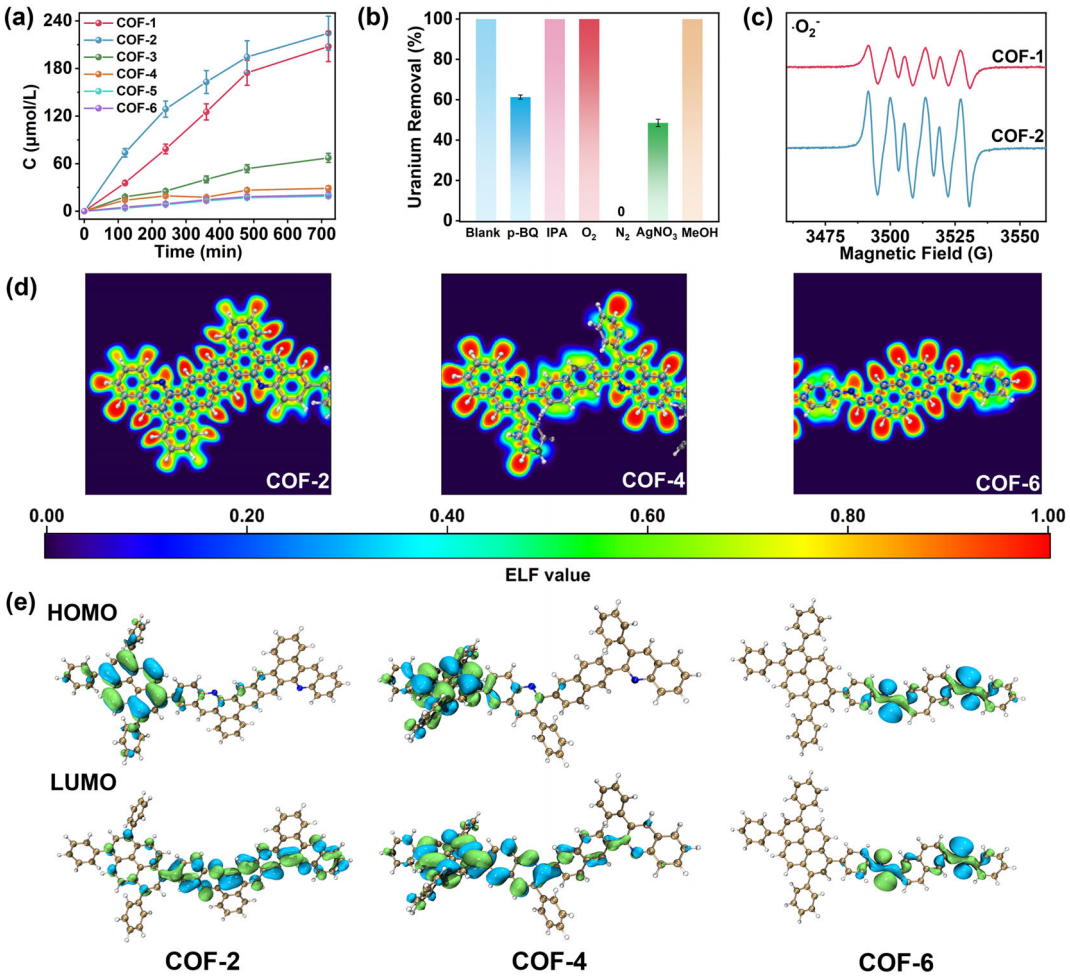


FIGURE 6 | Uranium extraction mechanism. (a) Photocatalytic H_2O_2 production performance of COF-1 to COF-6 in deionized water. (b) Quenching experiments for photocatalysis. (c) EPR spectra for $\cdot O_2^-$-DMPO adducts formed under visible light irradiation of COF-1 and COF-2. (d) The ELF diagrams of COF-2, COF-4, and COF-6. (e) LUMO and HOMO frontier molecular orbitals for the models of COF-2, COF-4, and COF-6.

the relationship between conjugated structures of the COFs and their photocatalytic performance. It should be noted that DFT calculations were carried out on idealized, periodic COF models, which may not explicitly replicate the real surface environment experienced by the COFs during photocatalytic tests. First, the electron localization function (ELF) provides a visual representation of the spatial distribution of electron pairs (Figure 6d; Figure S24), with values color-coded from blue (ELF ≈ 0, indicating delocalized electrons) to red (ELF ≈ 1, indicating highly localized electrons) [65]. In comparison to COF-3, COF-4, COF-5, and COF-6, the ELF plots show more delocalized electrons in the units of COF-1 and COF-2, reflecting their planarity and extended conjugation within the covalent network. Extended π-conjugated structures with fewer localized electrons (i.e., more delocalized electrons) facilitate photogenerated electron transfer, thereby enhancing photocatalytic activity. The electrostatic potential (ESP) maps provide complementary evidence of the degree of electron delocalization and reveal how the conjugation regime influences charge distribution at the molecular level in the COF fragments (Figure S25). The negative electrostatic potential is distributed as a smooth and broad region across the entire polycyclic aromatic unit and the cyclized linkages of COF-1 (COF-2). This uniform and continuous charge distribution demonstrates that electrons are not confined to specific atoms or small groups but are free to delocalize throughout the entire π-system. In the ESP map of COF-3 (COF-4), the negative potential cannot transition smoothly between different aromatic units due to the non-planar conformation of the quinoline linkage. This fragmented charge distribution illustrates that the non-planar structure disrupts long-range conjugation, limiting electron delocalization across the framework. For COF-5 (COF-6), the negative electrostatic potential is highly concentrated around the imine nitrogen atom in the ESP maps, and electrons are confined to the electron-rich nitrogen site rather than delocalizing across the entire aromatic system. Extended π-conjugated COF-1 and COF-2, relying on enhanced linkages and planar structures possessing fewer localized electrons (i.e., more delocalized electrons), facilitate photogenerated electron transfer, thereby enhancing photocatalytic activity. The calculated molecular orbital distributions of COFs offered invaluable insights into charge-transfer characteristics (Figure 6e). The highest occupied molecular orbitals (HOMO) and the lowest unoccupied molecular orbitals (LUMO) for COFs exhibited different spatial distribution, revealing that COF-2 possesses significantly more pronounced HOMO-LUMO separation than COF-4 and COF-6 [66]. Benefiting from its inherent electron-donating tendency,

COF-2 exhibits HOMO concentrated on the pyrene units and LUMO localized on the polycyclic aromatic units, which act as electron-accepting sites. This finding implies that the enhanced π-conjugation is responsible for the superior electron-transport performance within the planar framework. In contrast, COF-4 and COF-6, which feature p-π conjugation, exhibit significant orbital overlap that prevents efficient electron-hole separation and suppresses charge transfer.

Taken together, both experimental and theoretical results demonstrate that extended π-conjugated COFs exhibit excellent photocatalytic performance. The extended π-conjugated frameworks (COF-1 and COF-2), characterized by polycyclic aromatic units, facilitate continuous π-electron delocalization and efficient electron transport compared to their imine-linked and imine-cyclized counterparts, as confirmed by U(VI) removal experiments conducted under various conditions. We anticipate that our proof-of-concept study will provide new insights into the synthesis of tailored COF photocatalysts for U(VI) removal from wastewater and other applications.

3 | Conclusion

In summary, a series of COF photocatalysts was successfully synthesized via an atom-level design strategy, with the relationship between their conjugated structures and photocatalytic performance elucidated. Both experimental findings and theoretical results indicate that extended π-conjugated structures benefit photocatalytic electron generation, separation, and transportation. The extended π-conjugated COFs synthesized in this work (COF-1 and COF-2) demonstrated superior photocatalytic activity for U(VI) removal under various conditions compared to their respective imine-linked counterparts and imine-cyclized structures with p-π conjugations. Notably, our newly developed COF-2 exhibited exceptional U(VI) removal efficiency in aqueous solutions under visible-light irradiation, yielding a solid $(UO_2)O_2{\cdot}4H_2O$ product. This study opens new avenues for designing COF-based photocatalysts with superior activity and chemical stability.

Acknowledgements

The authors gratefully acknowledge funding support from the National Natural Science Foundation of China (Grants No. 22322603, 22506048, and U24B20195), the Fundamental Research Funds for the Central Universities (2025MS052, 2026JC005), and the Robert A. Welch Foundation (B-0027). G.I.N.W. acknowledges funding support from the MacDiarmid Institute for Advanced Materials and Nanotechnology.

Conflicts of Interest

The authors declare no conflicts of interest.

Data Availability Statement

The data that supports the findings of this study are available in the supplementary material of this article.

References

1. A. P. Côté, A. I. Benin, N. W. Ockwig, et al., "Porous, Crystalline, Covalent Organic Frameworks," *Science* 310, no. 5751 (2005): 1166–1170, https://doi.org/10.1126/science.1120411.

2. H. M. El-Kaderi, J. R. Hunt, J. L. Mendoza-Corte?s, et al., "Designed Synthesis of 3D Covalent Organic Frameworks," *Science* 316, no. 5822 (2007): 268–272, https://doi.org/10.1126/science.1139915.

3. F. J. Uribe-Romo, J. R. Hunt, H. Furukawa, C. Klöck, M. O'Keeffe, and O. M. Yaghi, "A Crystalline Imine-Linked 3-D Porous Covalent Organic Framework," *Journal of the American Chemical Society* 131, no. 13 (2009): 4570–4571, https://doi.org/10.1021/ja8096256.

4. X. Zhao, P. Pachfule, and A. Thomas, "Covalent Organic Frameworks (COFs) for Electrochemical Applications," *Chemical Society Reviews* 50, no. 12 (2021): 6871–6913, https://doi.org/10.1039/d0cs01569e.

5. J. Zhang, H. Chen, C. Luo, et al., "Modulating Heterocyclic Linkages of Covalent Organic Frameworks to Expand Photocatalytic Uranium Extraction," *Carbon Research* 5 (2026): 29, https://doi.org/10.1007/s44246-026-00285-1.

6. L.-J. Wang, P.-Y. Dong, G. Zhang, and F.-M. Zhang, "Review and Perspectives of B-Keto-Enamine-Based Covalent Organic Framework for Photocatalytic Hydrogen Evolution," *Energy & Fuels* 37, no. 9 (2023): 6323–6347, https://doi.org/10.1021/acs.energyfuels.3c00162.

7. M. Hao, M. Lei, and J. Zhang, "Flexible Units in Covalent Organic Frameworks Promote Photocatalytic Uranium Extraction From Wastewater," (2026), 3528–3541, https://doi.org/10.31635/ccschem.025.202506940.

8. S. Manzoor, M. A. Younis, Y. Yao, et al., "Schiff Base COFs for Photocatalysis: From Fundamentals to Applications," *Coordination Chemistry Reviews* 541 (2025): 216840, https://doi.org/10.1016/j.ccr.2025.216840.

9. H. Wang, H. Wang, Z. Wang, et al., "Covalent Organic Framework Photocatalysts: Structures and Applications," *Chemical Society Reviews* 49 (2020): 4135–4165, https://doi.org/10.1039/d0cs00278j.

10. L. Ding, Z. Pan, and Q. Wang, "2D Photocatalysts for Hydrogen Peroxide Synthesis," *Chinese Chemical Letters* 35, no. 12 (2024): 110125, https://doi.org/10.1016/j.cclet.2024.110125.

11. Z. Wang, Z. Lin, S. Shen, W. Zhong, and S. Cao, "Advances in Designing Heterojunction Photocatalytic Materials," *Chinese Journal of Catalysis* 42, no. 5 (2021): 710–730, https://doi.org/10.1016/s1872-2067(20)63698-1.

12. W.-R. Cui, F.-F. Li, R.-H. Xu, et al., "Regenerable Covalent Organic Frameworks for Photo-Enhanced Uranium Adsorption From Seawater," *Angewandte Chemie International Edition* 59, no. 40 (2020): 17684–17690, https://doi.org/10.1002/anie.202007895.

13. Q. Lu, Y. Ma, H. Li, et al., "Postsynthetic Functionalization of Three-Dimensional Covalent Organic Frameworks for Selective Extraction of Lanthanide Ions," *Angewandte Chemie International Edition* 57, no. 21 (2018): 6042–6048, https://doi.org/10.1002/anie.201712246.

14. M. Hao, Y. Xie, Z. Chen, et al., "Promising Porous Materials for Uranium Extraction From Seawater," *Fundamental Research* 6, no. 1 (2026): 170–172, https://doi.org/10.1016/j.fmre.2024.03.004.

15. X. Yang, L. Gong, X. Liu, et al., "Mesoporous Polyimide-Linked Covalent Organic Framework With Multiple Redox-Active Sites for High-Performance Cathodic Li Storage," *Angewandte Chemie International Edition* 61, no. 31 (2022): 202207043, https://doi.org/10.1002/anie.202207043.

16. P. Wang, Y. Peng, C. Zhu, et al., "Single-Phase Covalent Organic Framework Staggered Stacking Nanosheet Membrane for CO 2 -Selective Separation," *Angewandte Chemie International Edition* 60, no. 35 (2021): 19047–19052, https://doi.org/10.1002/anie.202106346.

17. P. T. Parvatkar, S. Kandambeth, A. C. Shaikh, et al., "A Tailored COF for Visible-Light Photosynthesis of 2,3-Dihydrobenzofurans," *Journal of the American Chemical Society* 145, no. 9 (2023): 5074–5082, https://doi.org/10.1021/jacs.2c10471.

18. F. Xie, C. Bie, J. Sun, Z. Zhang, and B. Zhu, "A DFT Study on Pt Single Atom Loaded COF for Efficient Photocatalytic CO_2 Reduction," *Journal of Materials Science & Technology* 170 (2024): 87–94, https://doi.org/10.1016/j.jmst.2023.06.028.

19. K. Cai, W. Wang, J. Zhang, et al., "Facile Construction of Olefin-Linked Covalent Organic Frameworks for Enhanced Photocatalytic Organic Transformation via Wall Surface Engineering," *Journal of Materials Chemistry A* 10, no. 13 (2022): 7165–7172, https://doi.org/10.1039/d1ta09684b.

20. Q. Yang, M. Luo, K. Liu, H. Cao, and H. Yan, "Covalent Organic Frameworks for Photocatalytic Applications," *Applied Catalysis B: Environmental* 276 (2020): 119174, https://doi.org/10.1016/j.apcatb.2020.119174.

21. Y. Liu, H. Tan, Y. Wei, et al., "Cu_2O/2D COFs Core/Shell Nanocubes With Antiphotocorrosion Ability for Efficient Photocatalytic Hydrogen Evolution," *ACS Nano* 17, no. 6 (2023): 5994–6001, https://doi.org/10.1021/acsnano.3c00358.

22. B. B. Luan, X. Chu, Y. Wang, X. Qiao, Y. Jiang, and F. M. Zhang, "Construction of COF/COF Organic S-Scheme Heterostructure for Enhanced Overall Water Splitting," *Advanced Materials* 36, no. 49 (2024): 2412653, https://doi.org/10.1002/adma.202412653.

23. S. Ma, Z. Li, Y. Hou, et al., "Fully Conjugated Benzobisoxazole-Bridged Covalent Organic Frameworks for Boosting Photocatalytic Hydrogen Evolution," *Angewandte Chemie International Edition* 64, no. 19 (2025): 202501869, https://doi.org/10.1002/anie.202501869.

24. X. Dong, F. Zhang, Y. Wang, F. Huang, and X. Lang, "Selective Oxidation of Sulfides With Oxygen over a Pyrene Covalent Organic Framework Photocatalyst With Tempo," *Applied Catalysis B: Environment and Energy* 345 (2024): 123660, https://doi.org/10.1016/j.apcatb.2023.123660.

25. B. Mourino, K. M. Jablonka, A. Ortega-Guerrero, and B. Smit, "In Search of Covalent Organic Framework Photocatalysts: A DFT-Based Screening Approach," *Advanced Functional Materials* 33, no. 32 (2023): 2301594, https://doi.org/10.1002/adfm.202301594.

26. H.-X. He, C.-R. Zhang, X.-J. Chen, R.-P. Liang, and J.-D. Qiu, "Reconstruction of Built-in Electric Field in Covalent Organic Frameworks Through Defect Engineering for Photocatalytic Reduction of Uranium," *ACS Applied Polymer Materials* 7, no. 7 (2025): 4525–4534, https://doi.org/10.1021/acsapm.5c00178.

27. Z. Li, Z. Dong, Z. Zhang, et al., "Covalent Organic Frameworks for Boosting H_2O_2 Photosynthesis via the Synergy of Multiple Charge Transfer Channels and Polarized Field," *Angewandte Chemie International Edition* 64, no. 7 (2024): 202420218, https://doi.org/10.1002/anie.202420218.

28. L. Qin, C. Ma, J. Zhang, and T. Zhou, "Structural Motifs in Covalent Organic Frameworks for Photocatalysis," *Advanced Functional Materials* 34, no. 41 (2024): 2401562, https://doi.org/10.1002/adfm.202401562.

29. R. Bao, Z. Xiang, Z. Qiao, et al., "Designing Thiophene-Enriched Fully Conjugated 3D Covalent Organic Framework as Metal-Free Oxygen Reduction Catalyst for Hydrogen Fuel Cells," *Angewandte Chemie International Edition* 62, no. 4 (2022): 202216751, https://doi.org/10.1002/anie.202216751.

30. R. A. Borse, Y.-X. Tan, J. Lin, et al., "Coupling Electron Transfer and Redox Site in Boranil Covalent Organic Framework toward Boosting Photocatalytic Water Oxidation," *Angewandte Chemie International Edition* 63, no. 13 (2024): 202318136, https://doi.org/10.1002/anie.202318136.

31. R. Chen, J.-L. Shi, Y. Ma, G. Lin, X. Lang, and C. Wang, "Designed Synthesis of a 2D Porphyrin-Based sp 2 Carbon-Conjugated Covalent Organic Framework for Heterogeneous Photocatalysis," *Angewandte Chemie International Edition* 58, no. 19 (2019): 6430–6434, https://doi.org/10.1002/anie.201902543.

32. Y. Liang, M. Xia, Y. Zhao, et al., "Functionalized Triazine-Based Covalent Organic Frameworks Containing Quinoline via Aza-Diels-Alder Reaction for Enhanced Lithium-Sulfur Batteries Performance," *Journal of Colloid and Interface Science* 608 (2022): 652–661, https://doi.org/10.1016/j.jcis.2021.09.150.

33. X. Li, C. Zhang, S. Cai, et al., "Facile Transformation of Imine Covalent Organic Frameworks into Ultrastable Crystalline Porous Aromatic Frameworks," *Nature Communications* 9, no. 1 (2018): 2998, https://doi.org/10.1038/s41467-018-05462-4.

34. J. Thote, H. B. Aiyappa, A. Deshpande, D. Díaz Díaz, S. Kurungot, and R. Banerjee, "A Covalent Organic Framework–Cadmium Sulfide Hybrid as a Prototype Photocatalyst for Visible-Light-Driven Hydrogen Production," *Chemistry—A European Journal* 20, no. 48 (2014): 15961–15965, https://doi.org/10.1002/chem.201403800.

35. Q. Zhu, L. Shi, Z. Li, G. Li, and X. Xu, "Protonation of an Imine-Linked Covalent Organic Framework for Efficient H 2 O 2 Photosynthesis Under Visible Light up to 700 nm," *Angewandte Chemie International Edition* 63, no. 32 (2024): 202408041, https://doi.org/10.1002/anie.202408041.

36. L. Fang, H. Xu, S. Qiu, et al., "Autocatalytic Interfacial Synthesis of Self-Standing Amide-Linked Covalent Organic Framework Membranes," *Angewandte Chemie International Edition* 64, no. 13 (2025): 202423220, https://doi.org/10.1002/anie.202423220.

37. L. Wang, D. Ma, A. Liu, et al., "Asymmetric Diamine Synthesis for Covalent Organic Frameworks: Boosted Photocatalytic Performance by Restricting β-Ketoenamine Bond Twist," *Angewandte Chemie International Edition* 64, no. 47 (2025): 202518097, https://doi.org/10.1002/anie.202518097.

38. E. Jin, M. Asada, Q. Xu, et al., "Two-Dimensional sp 2 Carbon–Conjugated Covalent Organic Frameworks," *Science* 357, no. 6352 (2017): 673–676, https://doi.org/10.1126/science.aan0202.

39. X. Zhuang, W. Zhao, F. Zhang, et al., "A Two-Dimensional Conjugated Polymer Framework With Fully sp^2-Bonded Carbon Skeleton," *Polymer Chemistry* 7, no. 25 (2016): 4176–4181, https://doi.org/10.1039/c6py00561f.

40. S.-Y. Ding, J. Gao, Q. Wang, et al., "Construction of Covalent Organic Framework for Catalysis: Pd/COF-LZU1 in Suzuki–Miyaura Coupling Reaction," *Journal of the American Chemical Society* 133, no. 49 (2011): 19816–19822, https://doi.org/10.1021/ja206846p.

41. L. Zou, R. Sa, H. Zhong, H. Lv, X. Wang, and R. Wang, "Photoelectron Transfer Mediated by the Interfacial Electron Effects for Boosting Visible-Light-Driven CO_2 Reduction," *ACS catalysis* 12, no. 6 (2022): 3550–3557, https://doi.org/10.1021/acscatal.1c05449.

42. P.-F. Wei, M.-Z. Qi, Z.-P. Wang, et al., "Benzoxazole-Linked Ultrastable Covalent Organic Frameworks for Photocatalysis," *Journal of the American Chemical Society* 140, no. 13 (2018): 4623–4631, https://doi.org/10.1021/jacs.8b00571.

43. H. Yang, M. Hao, Y. Xie, et al., "Tuning Local Charge Distribution in Multicomponent Covalent Organic Frameworks for Dramatically Enhanced Photocatalytic Uranium Extraction," *Angewandte Chemie International Edition* 62, no. 30 (2023): 202303129, https://doi.org/10.1002/anie.202303129.

44. S. Yang, Z. Chen, L. Zou, and R. Cao, "Construction of Thiadiazole-Linked Covalent Organic Frameworks via Facile Linkage Conversion With Superior Photocatalytic Properties," *Advanced Science* 10, no. 31 (2023): 2304697, https://doi.org/10.1002/advs.202304697.

45. T.-X. Luan, L.-B. Xing, N. Lu, et al., "Donor–Acceptor-π-Acceptor–Donor-Type Photosensitive Covalent Organic Framework for Effective Photocatalytic Aerobic Oxidation," *Journal of the American Chemical Society* 147, no. 15 (2025): 12704–12714, https://doi.org/10.1021/jacs.5c00750.

46. C. He, S. Tao, R. Liu, Y. Zhi, and D. Jiang, "Covalent Organic Frameworks: Linkage Chemistry and Its Critical Role in the Evolution of π Electronic Structures and Functions," *Angewandte Chemie International Edition* 63, no. 22 (2024): 202403472, https://doi.org/10.1002/anie.202403472.

47. S. Bi, C. Yang, W. Zhang, et al., "Two-Dimensional Semiconducting Covalent Organic Frameworks via Condensation at Arylmethyl Carbon Atoms," *Nature Communications* 10, no. 1 (2019): 2467, https://doi.org/10.1038/s41467-019-10504-6.

48. Y. Wang, H. Liu, Q. Pan, et al., "Construction of Fully Conjugated Covalent Organic Frameworks via Facile Linkage Conversion for Efficient Photoenzymatic Catalysis," *Journal of the American Chemical Society* 142, no. 13 (2020): 5958–5963, https://doi.org/10.1021/jacs.0c00923.

49. D. Huang, Y. Zhang, H. Pang, X. Hu, and Y. Xiang, "Ionization-Triggered Low Exciton Binding Energy in Covalent Organic Frameworks for Efficient Photocatalytic Synthesis of Benzimidazole," *Journal of Materials Chemistry A* 12, no. 29 (2024): 18512–18518, https://doi.org/10.1039/d4ta02824d.

50. Z. Xiao, X. Nie, Y. Li, Y. Nie, L. Lu, and X. Tian, "Boric Acid Functional Fluorescent Covalent-Organic Framework for Sensitive and Selective Visualization of CH_3Hg^+," *ACS Applied Materials & Interfaces* 15, no. 7 (2023): 9524–9532, https://doi.org/10.1021/acsami.2c23302.

51. H. Chen, W. Liu, C. Liu, et al., "Two in One: A Brønsted Acid Grafted Photoactive Covalent Organic Framework as Metal-Free Dual Photocatalyst for Aerobic Oxidative C-C Cleavage," *Applied Catalysis B: Environmental* 319 (2022): 121920, https://doi.org/10.1016/j.apcatb.2022.121920.

52. H. Xu, Y. Wang, Y. Xu, et al., "Integrating Multipolar Structures and Carboxyl Groups in sp 2 -Carbon Conjugated Covalent Organic Frameworks for Overall Photocatalytic Hydrogen Peroxide Production," *Angewandte Chemie International Edition* 63, no. 41 (2024): 202408802, https://doi.org/10.1002/anie.202408802.

53. M. Lenzen, "Life Cycle Energy and Greenhouse Gas Emissions of Nuclear Energy: A Review," *Energy Conversion and Management* 49, no. 8 (2008): 2178–2199, https://doi.org/10.1016/j.enconman.2008.01.033.

54. S. Zhou and X. Zhang, "Nuclear Energy Development in China: A Study of Opportunities and Challenges," *Energy* 35, no. 11 (2010): 4282–4288, https://doi.org/10.1016/j.energy.2009.04.020.

55. Z. Wang, Q. Meng, R. Ma, et al., "Constructing an Ion Pathway for Uranium Extraction From Seawater," *Chemistry* 7 (2020): 1683–1691, https://doi.org/10.1016/j.chempr.2020.04.012.

56. A. Ashish, P. Bangotra, V. Dillu, et al., "Human Exposure to Uranium Through Drinking Water and Its Detrimental Impact on the Human Body Organs," *Environmental Geochemistry and Health* 46, no. 10 (2024): 397, https://doi.org/10.1007/s10653-024-02150-9.

57. M. Ma, R. Wang, L. Xu, M. Xu, and S. Liu, "Emerging Health Risks and Underlying Toxicological Mechanisms of Uranium Contamination: Lessons From the Past Two Decades," *Environment International* 145 (2020): 106107, https://doi.org/10.1016/j.envint.2020.106107.

58. S. Zhao, T. Feng, M. Cao, T. Liu, Y. Yuan, and N. Wang, "Ferrocene-Based 2D Metal–Organic Framework Nanosheet for Highly Efficient Photocatalytic Seawater Uranium Recovery," *Chemical Engineering Journal* 498 (2024): 155228, https://doi.org/10.1016/j.cej.2024.155228.

59. B. Chen, G. Zhang, L. Chen, et al., "Visible Light Driven Photocatalytic Removal of Uranium(VI) in Strongly Acidic Solution," *Journal of Hazardous Materials* 426 (2022): 127851, https://doi.org/10.1016/j.jhazmat.2021.127851.

60. S. Han, W. Liang, H. Wan, et al., "Vascular-Mimetic 2D Membranes With Hemoglobin Catalysis for Efficient Uranium Extraction," *Advanced Materials* 38, no. 1 (2026): 09989, https://doi.org/10.1002/adma.202509989.

61. P. Gao, Y. Hu, Z. Shen, et al., "Ultra-Highly Efficient Enrichment of Uranium from Seawater via Studtite Nanodots Growth-Elution Cycle," *Nature Communications* 15 (2024): 6700, https://doi.org/10.1038/s41467-024-50951-4.

62. J. Qiu, C. Cheng, H. García, et al., "Metal-Free Singlet Oxygen Generation via Excited-State Intramolecular Proton-Transfer-Driven Intersystem Crossing in 2D Covalent Organic Frameworks," *Angewandte Chemie International Edition* 64, no. 50 (2025): 202515898, https://doi.org/10.1002/anie.202515898.

63. H. Zhang, R. Ma, K. Chi, Y. Liu, and Y. Zhao, "Hydrogen Radical Mediated Concerted Electron-Proton Transfer in 1D Sulfone-Based Covalent Organic Framework for Boosting Photosynthesis of H_2O_2," *Angewandte Chemie International Edition* 64, no. 44 (2025): 202516657, https://doi.org/10.1002/anie.202516657.

64. R. Guo, Y. Huo, L. Song, et al., "Hydroxyl-Based Donor-Acceptor Covalent Triazine Frameworks as Efficient Platforms for in-Situ Photocatalytic U(VI) Reduction," *Applied Catalysis B: Environment and Energy* 365 (2025): 124950, https://doi.org/10.1016/j.apcatb.2024.124950.

65. X. Feng, X. Liang, X. Li, et al., "Improving the Response of 2D COFs to the Surface Doping Strategies Through Rational Design of Their Chemical Structure," *Science China Materials* 10 (2024): 3272–3281, https://doi.org/10.1007/s40843-024-3032-7.

66. X. Liu, Z. Zhang, Q. Zhang, et al., "Tris(Triazolo)Triazine-Based Covalent Organic Frameworks for Efficiently Photocatalytic Hydrogen Peroxide Production," *Angewandte Chemie International Edition* 63, no. 45 (2024): 202411546, https://doi.org/10.1002/anie.202411546.

Supporting Information

Additional supporting information can be found online in the Supporting Information section.

Supporting File: smll74554-sup-0001-SuppMat.pdf.